Template banks based on $\mathbb{Z}^n$ and A_n^* lattices

Bruce Allen[*] and Andrey A. Shoom[†]

Max Planck Institute for Gravitational Physics (Albert Einstein Institute), Leibniz Universität Hannover, Callinstrasse 38, D-30167 Hannover, Germany

(Received 7 July 2021; accepted 19 October 2021; published 28 December 2021)

Matched filtering is a traditional method used to search a data stream for signals. If the source (and hence its n parameters) are unknown, many filters must be employed. These form a grid in the n-dimensional parameter space, known as a template bank. It is often convenient to construct these grids as lattices. The simplest of these, $\mathbb{Z}^n$, is used in both continuous gravitational-wave and gamma-ray pulsar searches; we wanted to investigate how much might be gained by replacing it with the more elaborate A_n^* lattice. To determine this, we calculate the distribution of the mismatch function, both in the traditional quadratic approximation and with the recently proposed spherical ansatz. The fraction of signals which are lost is determined by the even moments of this distribution, which we find. Many of these quantities have a simple and well-defined $n \to \infty$ limit, which often gives an accurate estimate even for small n. Our main conclusions are the following: (i) a fairly effective template-based search can be constructed at mismatch values that are shockingly high in the quadratic approximation; (ii) the minor advantage offered by an A_n^* template bank (compared to $\mathbb{Z}^n$) at small template separation becomes even less significant for large template spacings. In most cases, the gain from employing an A_n^* lattice is not enough to justify the increase in complexity.

DOI: 10.1103/PhysRevD.104.122007

I. INTRODUCTION

Matched filtering is a standard technique [1,2] used to search for weak gravitational-wave signals from the binary inspiral of black holes and/or neutron stars. This compares the data (suitably weighted in frequency space) to a template of the expected waveform [3–14]. Matched filtering is also used to search for weak electromagnetic (radio and gamma-ray) [15] and gravitational-wave signals from rapidly rotating neutron stars (pulsars) [16] and has many other applications across a broad range of fields and topics.

Because these searches are typically looking for new events and/or unknown sources, the parameters of the signals are not known. Some examples of these parameters include sky position, mass, and spin or chirp frequency. Thus, a collection of templates must be employed. The grid of these templates in parameter space is generally referred to as a "template bank."

If the parameter space is low dimensional and the volume of interest is not too large, one can simply "overcover" the space, by putting many redundant templates close together. However, if the parameter-space dimension and/or volume is large, this quickly becomes (computationally speaking) very expensive. On the other hand, if the templates are spaced too far apart, then it is possible that some signals could be missed, because there are no templates in the bank which match the waveforms closely enough. Thus, a compromise must be reached: enough templates must be employed that signals are not lost, but their number must not be so large that the computing cost explodes. For some searches (e.g., for continuous gravitational waves from neutron stars in binary systems) the computing cost is so high that it constrains the search sensitivity.

The problem of how to place templates in parameter space is well studied. There are many ways to construct template banks. For example, one can simply place the templates at random [17], with a high enough density that most signals are likely to lie near enough to a template. Or one can improve this by removing redundant templates which are "too close" to neighboring ones, and adding more templates at random, if required [18]. One can also build template banks as lattices in parameter space.

Following this approach, two important lattices are $\mathbb{Z}^n$ and A_n^*. The first is the Cartesian product of equally spaced grids in all dimensions, and the second is the n-dimensional generalization of the two-dimensional hexagonal lattice and the three-dimensional fcc lattice. Both are used in large-parameter-space searches. For example

[*]bruce.allen@aei.mpg.de
[†]andrey.shoom@aei.mpg.de

the Einstein@Home all-sky searches for continuous gravitational waves use a $\mathbb{Z}^4$ template bank [19,20]; the four parameters are frequency f, its time derivative $\dot{f}$, and the projections of the sky position onto a Cartesian plane containing Earth's orbit about the Sun, (n_x, n_y). A recent targeted Einstein@Home search [21] used $\mathbb{Z}^3$, where the three parameters are f, $\dot{f}$ and $\ddot{f}$. Searches for gamma-ray pulsars use both types of lattices. For example, the first stage of searches that recently discovered two "spider" pulsars [22,23] employ a $\mathbb{Z}^2$ lattice for $(f, \dot{f})$ and an A_2^* lattice for sky position. In the follow-up stage, a $\mathbb{Z}^5$ lattice is used for f, $\dot{f}$, P, a, T; the final three parameters are orbital period, projected semimajor axis, and time of the ascending node [15]). Some related searches, for example [24], only use $\mathbb{Z}^5$, because they only contain the follow-up stage. Part of the motivation for this work was to investigate if replacing $\mathbb{Z}^n$ with A_n^* might significantly increase the discovery rate in such searches.

More broadly, lattices provide a standard for comparison. Since the *optimal quantizer* lattice is superior to any other choice of template bank (under reasonable assumptions it maximizes the number of detections for a given number of templates [25]) it provides a "gold standard." Thus, the analytic results presented here provide a comparison for any template bank, and allow designers to bound potential improvements to their banks, particularly when the worst-case mismatch is very large.

One way to characterize a template bank is via the mismatch function m. This is a function on parameter space, which quantifies how much signal-to-noise ratio (SNR) is lost because of the discreteness of the template bank. Its value at any point is the fractional difference between the squared SNR obtained for a signal with those parameters in the nearest template, and the squared SNR that would have been obtained had a template been located *exactly* at that point. Thus, m vanishes at the locations of the templates, and is largest "halfway in between" two templates. In a recent paper, we showed how the fraction of lost signals is related to the average of m and functions of m [25].

Note that in the literature, the term "mismatch" is sometimes used differently than we do here. In some cases, it refers to the worst-case mismatch, meaning the maximum value of our function. In other cases, it is a function of two points of parameter space. In this paper, we follow [25]: m is a function of a single point in parameter space. Our definition corresponds to Eq. (2.5) of [25], as illustrated in Fig. 1 of that paper.

When the templates are close together, so the mismatch is small, m can be expressed as a positive-definite quadratic form and thought of as the squared distance between the parameter-space point with the coordinates λ^a and the closest template. Thus, in this approximation, $m \approx g_{ab}\Delta\lambda^a\Delta\lambda^b$, where g_{ab} is the metric on the parameter space, $\Delta\lambda^a$ is the coordinate separation between the point and the closest template (see, e.g., [13,26]), and we adopt the "summation convention" that repeated indices are summed from 1 to n. In this paper, we call this the quadratic approximation to the mismatch, and write it as $m = r^2$.

When the templates are less-closely spaced, a better approximation to the mismatch is the "spherical" ansatz, $m \approx \sin^2 r = \sin^2(\sqrt{g_{ab}\Delta\lambda^a\Delta\lambda^b})$, recently introduced in [27]. The spherical ansatz could also be used for the semicoherent mismatch, thus providing a tractable alternative to more complicated approaches such as the averaged metric of [28].

In general, the parameter-space metric g_{ab} is a function of the coordinates λ^a. In what follows, we will assume that the parameter space has been divided into regions which are large enough that they contain many templates, but small enough that g_{ab} can be treated as a constant within each region. For example, in a search for continuous gravitational waves, a 1-kHz frequency interval might be broken into 1-Hz bands. (Within these, typical template spacings might be a fraction of a μHz.) Then, in each region, by diagonalization and rescaling, we introduce new coordinates x_i, for which $r^2 = g_{ab}\Delta\lambda^a\Delta\lambda^b = \Delta x_1^2 + \cdots + \Delta x_n^2$.

Another good example is the search for gamma-ray pulsations from isolated neutron stars with a linear spin-down. This is a four-dimensional parameter space whose coordinates are frequency f, frequency derivative $\dot{f}$, and sky position coordinates (n_x, n_y). For typical multiyear datasets, it can be seen from Eqs. (28) and (29) in [15] that the metric only depends upon f. So, provided that the parameter space is broken into regions which cover small ranges of frequency (say from f to $1.1f$) the metric can be treated as a constant. (This also holds for the semicoherent metric; see Eq. (42) in [15].)

If the mismatch is small, then the bank which minimizes the average value of r^2 loses the smallest fraction of signals [25]. If the bank is a lattice, this is called the "optimal quantizer" [29]. This paper extends those results to large mismatch, by exploiting the spherical ansatz [27] and carrying out an explicit calculation for template banks constructed from the $\mathbb{Z}^n$ and A_n^* lattices.

Our paper is organized as follows. In Sec. II we describe the n-dimensional lattices $\mathbb{Z}^n$ and A_n^*, and derive their key properties. In Sec. III we calculate the fraction of lost detections using the quadratic approximation and spherical ansatz for these lattices for two- and three-dimensional source distribution. This fraction of lost signals may be thought of as the "inefficiency" or "loss fraction" of the lattice. In Sec. IV we evaluate the loss fraction as the parameter-space dimension $n \to \infty$. This gives us simple analytic expressions; in some cases the approach is fast enough that these are good approximations even in finite numbers of dimensions. In Sec. V we compare the loss fraction of $\mathbb{Z}^n$ and A_n^* at fixed numbers of templates (which for simple one-stage searches is equivalent to fixed

computing cost). Finally, in Sec. VI, we derive the distribution function of the squared radius r^2 and examine its properties for the $\mathbb{Z}^n$ and A_n^* lattices. This is followed by a short conclusion.

Our results only depend on the even-order moments of the Wigner-Seitz (WS) cells of the lattices, which we denote by $\langle r^{2m}\rangle$. Appendix A contains a calculation of these moments for the $\mathbb{Z}^n$ lattice and Appendix B contains the corresponding calculation for the A_n^* lattice.

II. THE $\mathbb{Z}^n$ AND A_n^* LATTICES

The lattices $\mathbb{Z}^n$ and the A_n^* are an infinite collection of regularly spaced points in Cartesian space $\mathbb{R}^n$. We use $\boldsymbol{x}$ to denote a point in $\mathbb{R}^n$ with the normal Euclidean norm $|\boldsymbol{x}|^2 = \boldsymbol{x}\cdot\boldsymbol{x}$, where the dot denotes the standard dot product. The lattices are generated by a set of n constant basis vectors $\boldsymbol{e}_i \in \mathbb{R}^n$, for $i \in 1,\ldots,n$, which for these particular lattices are normalized so that $\boldsymbol{e}_i\cdot\boldsymbol{e}_i = 1$. Two-dimensional representatives of these lattices are illustrated in Fig. 1.

To characterize the geometry of the lattice, we shall use x_i to denote Cartesian coordinates and y_i to denote lattice coordinates. Accordingly, the lattice consists of all points $\boldsymbol{x} = y_i\boldsymbol{e}_i$ in $\mathbb{R}^n$, such that $y_i = c_i\ell$, where $c_i \in \mathbb{Z}$ are integers and ℓ is the lattice spacing. As earlier, we follow the "summation convention" that repeated indices are summed.

The squared distance r^2 between points $\boldsymbol{x}_A$ and $\boldsymbol{x}_B$ with lattice coordinates y_{Ai} and y_{Bi} is then

$$r^2 = (\boldsymbol{x}_A - \boldsymbol{x}_B)\cdot(\boldsymbol{x}_A - \boldsymbol{x}_B) = \Delta y_i \Delta y_j \boldsymbol{e}_i\cdot\boldsymbol{e}_j = g_{ij}\Delta y_i \Delta y_j, \tag{2.1}$$

where $\Delta y_i = y_{Ai} - y_{Bi}$ are the lattice coordinate separations and $g_{ij} = \boldsymbol{e}_i\cdot\boldsymbol{e}_j$ is a Gram matrix (see, e.g., [29]).

The region of $\mathbb{R}^n$ for which the coordinates $y_i \in [0,\ell]$ is called a "Fundamental Polytope" or FP. The FP has 2^n vertices, which are neighboring lattice points. The region of $\mathbb{R}^n$ which is closer [in the sense of the coordinate distance Eq. (2.1)] to a given lattice point than to any other lattice point is called the "WS cell" of that lattice point. We denote the Wigner-Seitz cell of the origin $y_i = 0$ by WS (see Fig. 1). The distance from the origin to the most distant point of WS is called the covering radius or WS radius R; it is the radius of the smallest sphere about the origin which encloses every point of the WS.

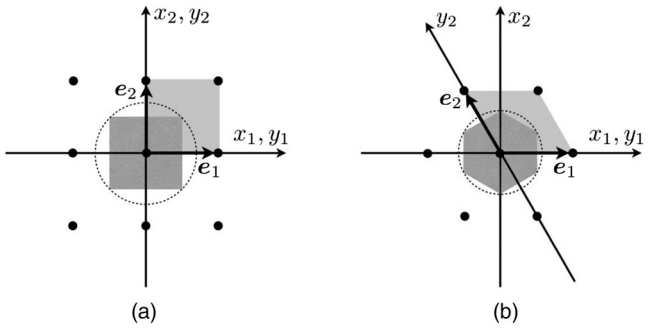

FIG. 1. Two-dimensional lattices: (a) the $\mathbb{Z}^2$ square lattice, (b) the A_2^* hexagonal lattice. The fundamental polytopes are shown in light gray; the WS cells are shown in dark gray and inscribed by the dashed circles of the covering radius. For general n, the basis vectors $\boldsymbol{e}_i$ for A_n^* define vertices of an equilateral n-simplex [see text after Eq. (2.10)].

We can compute the n-volume of the FP and the WS as follows. Since all FP are equivalent, we concentrate on the FP defined by lattice coordinate values $y_i \in [0,\ell]$. The n-volume of the FP is

$$V_{\mathrm{FP}} = \int_0^\ell dy_1 \cdots \int_0^\ell dy_n \sqrt{g} = \ell^n\sqrt{g}, \tag{2.2}$$

where $g = \det(g_{ij}) = \mathrm{const}$. The n-volume of the WS, V_{WS}, is equal to that of the FP, because (if the WS is copied around all lattice points) they overlap only on the boundaries (a set of measure zero), are in one-to-one correspondence, and cover all of space.

The FP is contractible to the origin, in the sense that if a point $\boldsymbol{x} \in \mathbb{R}^n$ lies inside it, then so does the point $\lambda\boldsymbol{x}$ for $\lambda \in [0,1)$. Because it is defined via a linear construction, it can also be contracted to any other vertex, so it is convex and contractible in any direction. By construction the FP is bounded by a set of $(n-1)$-dimensional planes.

In similar fashion, the boundary of the WS is defined by a set of $(n-1)$-dimensional planes that lie halfway between the origin and the surrounding lattice points. We can compute the covering radius R of the WS centered at the origin by considering the subset of those planes which lie in the FP, i.e., which lie halfway between the origin and the remaining $2^n - 1$ FP lattice points, and finding the point of intersection most distant from the origin.

To characterize the efficiency of the space covering, one defines the thickness Θ as the average number of covering spheres that contain a point of the space. This is equal to the ratio of volume of an n-dimensional ball enclosed by one of the spheres, to the volume $V_{\mathrm{FP}} = V_{\mathrm{WS}}$ [29],

$$\Theta = \frac{V(B_n(R))}{V_{\mathrm{WS}}}. \tag{2.3}$$

Here, $V(B_n(R)) = \pi^{n/2}R^n/\Gamma(1+n/2)$ is the volume of an n-ball B_n of radius R. From the definition it follows that $\Theta \geq 1$. Smaller values of Θ indicate less overlap among the balls, i.e., a more efficient covering.[1]

In the following subsections we compute the quantities defined above for the $\mathbb{Z}^n$ and A_n^* lattices. We will use these quantities in calculating the statistical properties of

[1]Another quantity used in the literature is the normalized thickness (or center density) $\theta = R^n/V_{\mathrm{WS}}$.

functions of the distance, such as the mismatch, for both lattices and to compare the derived results.

A. The $\mathbb{Z}^n$ lattice

The $\mathbb{Z}^n$ lattice (see, e.g., [29]) is generated by orthonormal basis vectors:

$$\boldsymbol{e}_i \cdot \boldsymbol{e}_j = \delta_{ij}, \tag{2.4}$$

where δ_{ij} is the Kronecker delta, i.e., the Gram matrix g_{ij} is the identity matrix. Thus, if the basis vectors are taken as the standard coordinate basis, then the lattice coordinates y_i are just the normal Cartesian coordinates and $x_i = y_i$. The distance function Eq. (2.1) is

$$r^2 = \sum_{i=1}^{n} \Delta y_i^2, \tag{2.5}$$

and, according to Eq. (2.2), the n-volume of the FP is

$$V_{\mathrm{FP}} = \ell^n. \tag{2.6}$$

According to Eq. (2.1), the largest distance between any pair of vertices in the FP is $r^2 = n\ell^2$. It is also the largest distance from the origin to a point within the FP.

To find the boundary of the WS centered at the origin, we begin by finding the equations of the planes that lie halfway between the origin and the nearest lattice points at distance ℓ from the origin. (The other potential bounding planes are irrelevant because they lie outside.) There are $2n$ of these nearest lattice points. They have coordinates $(0, \ldots, 0, \pm\ell, 0, \ldots, 0)$, where ℓ is located in the jth position and the remaining $n-1$ coordinates vanish. Using the distance function Eq. (2.5) we find that the coordinates in the $(n-1)$-dimensional boundary planes satisfy the equation

$$\sum_{i=1}^{n} y_i^2 = (y_j \mp \ell)^2 + \sum_{\substack{i=1 \\ (i\neq j)}}^{n} y_i^2 = \ell^2 \mp 2\ell y_j + \sum_{i=1}^{n} y_i^2.$$

Thus the planes bounding the WS satisfy

$$y_j = \pm\ell/2. \tag{2.7}$$

There are $2n$ such planes, since $j = 1, \ldots, n$. These define an n-cube which is identical to the FP but shifted by $-\ell/2$ along each coordinate axis, so that its center is at the origin. Note that the result Eq. (2.7) follows directly from the lattice geometry.

The WS radius R is easily computed. The point of mutual intersection of the n planes with $y_j > 0$ defines a vertex of the WS. All of the 2^n vertices of the WS (defined by intersecting each of the possible planes, one for each coordinate, n in total) are at the same distance R from the origin. Hence, the WS covering radius R is the distance of that WS vertex from the origin. Using the expression Eq. (2.5) gives

$$R^2 = \frac{1}{4} n\ell^2 \tag{2.8}$$

for the covering radius of the $\mathbb{Z}^n$ lattice. The n-volume of the FP and of the WS can be expressed in terms of R, as

$$V_{\mathrm{FP}} = V_{\mathrm{WS}}^{\mathbb{Z}^n} = 2^n n^{-n/2} R^n. \tag{2.9}$$

Later, we will compare the properties of different lattices at fixed V_{WS}.

B. The A_n^* lattice

The A_n^* lattice is a classical root lattice, whose attractions have been discussed in detail by [30]. For $n \leq 17$ it is either the thinnest classical root lattice, or close to the thinnest one. (Note however that thinner nonclassical lattices have been constructed numerically, by semidefinite optimization in the space of lattices. The current record holders are listed in Table 2 of [31].)

The A_n^* lattice is generated by basis vectors chosen to satisfy (see, e.g., [29,32])

$$\boldsymbol{e}_i \cdot \boldsymbol{e}_j = \begin{cases} 1 & \text{for } i = j \\ -1/n & \text{for } i \neq j. \end{cases} \tag{2.10}$$

The vectors $\boldsymbol{e}_i$ are easily visualized: they point from the origin to n of the $n+1$ vertices of an equilateral n-simplex. (The unit vector from the origin to the final vertex of the simplex is $-\boldsymbol{e}_1 - \cdots - \boldsymbol{e}_n$, which implies that the center of the simplex lies at the origin of coordinates.)

For this lattice, the distance function Eq. (2.1) is

$$\begin{aligned} r^2 &= \sum_{i=1}^{n} \Delta y_i^2 - \frac{1}{n} \sum_{\substack{i,j=1 \\ (i\neq j)}}^{n} \Delta y_i \Delta y_j, \\ &= \left(1 + \frac{1}{n}\right) \sum_{i=1}^{n} \Delta y_i^2 - \frac{1}{n} \left(\sum_{i=1}^{n} \Delta y_i\right)^2, \end{aligned} \tag{2.11}$$

and the Gram matrix is

$$g_{ij} = \begin{pmatrix} 1 & -1/n & \cdots & -1/n \\ -1/n & 1 & \cdots & -1/n \\ \vdots & \vdots & \ddots & \vdots \\ -1/n & -1/n & \cdots & 1 \end{pmatrix}. \tag{2.12}$$

Using recursion and row reduction, or applying Sylvester's theorem, it is easy to see that the determinant is

$$g = n^{-n}(n+1)^{n-1}. \tag{2.13}$$

From Eq. (2.2), one obtains

$$V_{\mathrm{FP}} = n^{-n/2}(n+1)^{(n-1)/2}\ell^n \tag{2.14}$$

for the n-volume of the FP.

We now compute the covering radius R, which is the distance from the origin to the most distant point of the WS centered at the origin. To find the boundary of the WS centered at the origin, we first find the equation of the plane that lies halfway between the origin and a lattice point with coordinates $y_i = (0,\ldots,0,\ell,\ldots,\ell)$, where the number of zeros is k and the number of ℓ's is $n-k$. We take this form for an FP vertex because it is sufficiently general, i.e., according to the distance function form Eq. (2.11), the coordinates can be permuted without changing the distance value. In contrast to the $\mathbb{Z}^n$ lattice, every FP vertex defines a WS boundary plane. After multiplying the squared distance by an overall factor of $n/(n+1)$, the coordinates in the planes satisfy the equation

$$\begin{aligned}&\sum_{i=1}^{n} y_i^2 - \frac{1}{n+1}\left(\sum_{i=1}^{n} y_i\right)^2 \\ &\quad = \sum_{i=1}^{k} y_i^2 + \sum_{i=k+1}^{n} (y_i-\ell)^2 \\ &\qquad - \frac{1}{n+1}\left(\sum_{i=1}^{k} y_i + \sum_{i=k+1}^{n}(y_i-\ell)\right)^2.\end{aligned} \tag{2.15}$$

This expression can be simplified, rearranged, and divided by $2\ell(n-k)/(n+1)$ to obtain

$$\sum_{i=1}^{n} y_i = \frac{n+1}{n-k}\sum_{i=k+1}^{n} y_i - \frac{k+1}{2}\ell. \tag{2.16}$$

Writing the (unity) coefficient of the lhs as $(n+1)/(n-k) - (k+1)/(n-k)$, and canceling the common terms in the sums, gives

$$\frac{n+1}{n-k}\sum_{i=1}^{k} y_i - \frac{k+1}{n-k}\sum_{i=1}^{n} y_i = -\frac{k+1}{2}\ell. \tag{2.17}$$

Multiplying this expression by $(n-k)/(k+1)$ yields the following formula, which defines the planes bounding the WS cell:

$$\sum_{i=1}^{n} y_i = \frac{n+1}{k+1}\sum_{i=1}^{k} y_i + \frac{n-k}{2}\ell. \tag{2.18}$$

Although we obtained this equation for a specific subset of vertices, it is trivial to obtain the corresponding equation for any vertex, by replacing the sum from 1 to k with a sum over any k of the coordinates. Changing the sign of ℓ gives the corresponding parallel plane bounding the WS on the other side of the origin. For this reason, the WS is sometimes called a "permutohedron" [29] and denoted P_n.

To obtain the covering radius R, we intersect a set of n bounding planes defined by Eq. (2.18), to identify a point at this radius in the WS. The $k=0$ equation implies

$$\sum_{i=1}^{n} y_i = \frac{n\ell}{2}. \tag{2.19}$$

The $k=1$ equation then implies $y_1 = \ell/(n+1)$. Combining these with the $k=2$ equation implies $y_2 = 2\ell/(n+1)$. Continuing in this fashion, intersecting all of the planes implies $y_i = i\ell/(n+1)$. The squared covering radius of the WS is thus given by

$$\begin{aligned}R^2 &= \left(1+\frac{1}{n}\right)\sum_{i=1}^{n} y_i^2 - \frac{1}{n}\left(\sum_{i=1}^{n} y_i\right)^2 \\ &= \left(1+\frac{1}{n}\right)\frac{\ell^2}{(n+1)^2}(1^2+\cdots+n^2) - \frac{1}{n}\left(\frac{n\ell}{2}\right)^2 \\ &= \frac{\ell^2}{n(n+1)}\frac{n(n+1)(2n+1)}{6} - \frac{n\ell^2}{4} \\ &= \frac{1}{12}(n+2)\ell^2.\end{aligned} \tag{2.20}$$

As before, we can express the WS n-volume in terms of R:

$$V_{\mathrm{WS}}^{A_n^*} = \left[\frac{12(n+1)}{n(n+2)}\right]^{n/2}(n+1)^{-1/2}R^n. \tag{2.21}$$

This will be useful later, when we compare lattices at fixed WS volume.

III. THE FRACTION OF LOST DETECTIONS

A template bank is discrete, so most points in parameter space do not have an exactly matching template. As a result, there is (on average) some loss of SNR from mismatch between signal and template, which (on average) results in lost detections. We quantify the number of lost detections following the treatment given in [25].

Assume that the detector or instrument is located within a cloud of sources, such as a galaxy. Each source emits a signal, which would produce a detector SNR ρ^2 in a perfectly matching template. Assume that the number of sources is sufficiently large that it may be treated as a continuous distribution. Then the number of sources dN with SNR in the interval $(\rho^2, \rho^2+d\rho^2)$ is

$$dN = P(\rho^2)d\rho^2, \tag{3.1}$$

where $P(\rho^2)$ is the number of sources per unit SNR interval. To calculate $P(\rho^2)$, we need to know how the

sources are distributed with (luminosity) distance L from the detector, and how the SNR ρ^2 depends upon L.

We assume that the sources are distant enough that the detector is in their radiation zone. For gravitational-wave sources, the gravitational-wave strain h is inversely proportional to the source-detector distance L, so that SNR $\rho^2 \sim h^2 \sim 1/L^2$ [14]. For electromagnetic sources, the SNR ρ^2 is proportional to intensity, which also scales $\sim 1/L^2$ (for example, see [15, Eq. (11)]) so the same relation holds. So in both cases, if there is a uniform $d = 2$- or $d =$ 3-dimensional Euclidean spatial distribution of sources, one has

$$dN \sim L^{d-1} dL \sim \rho^{-d-2} d\rho^2, \tag{3.2}$$

which implies that $P(\rho^2) \propto \rho^{-d-2}$.

Note that for simplicity, we have assumed that the distribution function does not depend upon the source parameters, but only upon its distance. This assumption can be dropped, as shown in Sec. VI of [25]. That section, and the Conclusion of that paper, also have further discussion regarding realistic spatial distributions of sources, which might (for example) correspond to fractional values of d. For example for Galactic neutron stars, the effective value of d is between 2 and 3; see [33,34].

To fully determine $P(\rho^2)$, let ρ_D^2 denote the SNR lower bound for confident detection: below this threshold, detector noise would produce too many false positives. We then obtain

$$P(\rho^2) = \frac{d}{2} \frac{N_D}{\rho^2} \left(\frac{\rho_D^2}{\rho^2} \right)^{d/2}, \tag{3.3}$$

where N_D is the total number of detectable sources in the SNR range $\rho^2 \in [\rho_D^2, \infty)$, assuming perfect signal-to-template match.

Due to the mismatch m between a source signal and the closest template, the actual SNR detection threshold is $\rho_D^2/(1-m)$, where $m \in [0, 1)$. This means that some signals fail to be detected, because their (perfect match) SNR lies in the interval $\rho^2 \in [\rho_D^2, \rho_D^2/(1-m)]$. The number of these "lost" signals is

$$N_{\text{lost}} = \frac{1}{V} \int \int_{\rho_D^2}^{\rho_D^2/(1-m)} P(\rho^2) d\rho^2 dV, \tag{3.4}$$

where $dV = d^n x = \sqrt{g} d^n y$ is the volume element of parameter space[2], and $V = \int dV$ is the total volume. Note that we need to integrate over the parameter space, because the mismatch function $m = m(x_i)$ depends on a point in the parameter space. Finally, by using the explicit form of $P(\rho^2)$ above we find the fraction of lost detections (see [25, Eq. (5.10)]),

$$\frac{N_{\text{lost}}}{N_D} = \frac{1}{V} \int (1 - (1-m)^{d/2}) dV. \tag{3.5}$$

Assuming that the template bank is a lattice and that the parameter space has much larger volume than a single WS cell, and using the spherical ansatz for the mismatch [27], we find that the fraction of lost detections is [25, Eq. (5.10)]

$$\frac{N_{\text{lost}}}{N_D} \approx \frac{1}{V_{\text{WS}}} \int_{\text{WS}} f(r) dV, \tag{3.6}$$

where the integral is over a single WS cell, and the integrand (using the spherical ansatz) is

$$f(r) = \begin{cases} 1 - \cos^d r & \text{for } r \le \pi/2 \\ 1 & \text{for } r > \pi/2 \end{cases}. \tag{3.7}$$

The ratio N_{lost}/N_D defines the "loss fraction" of the lattice, i.e., the fraction of potentially detectable signals which the lattice fails to catch. Equivalently, $1 - N_{\text{lost}}/N_D$ is the efficiency of the lattice: the expected fraction of potentially detectable signals which are indeed found.

Provided that the WS cell is not too large, so that $R < \pi/2$, the integrand can be expanded in a series, giving a loss fraction

$$\begin{aligned} \frac{N_{\text{lost}}}{N_D} &\approx \frac{1}{V_{\text{WS}}} \int_{\text{WS}} (1 - \cos^d(r)) dV \\ &= \frac{d}{2} \langle r^2 \rangle - \frac{d(3d-2)}{24} \langle r^4 \rangle + \frac{d(15d^2 - 30d + 16)}{720} \langle r^6 \rangle \\ &\quad - \frac{d(105d^3 - 420d^2 + 588d - 272)}{40320} \langle r^8 \rangle + \cdots. \end{aligned} \tag{3.8}$$

Here,

$$\langle r^p \rangle = \frac{1}{V_{\text{WS}}} \int_{\text{WS}} r^p dV \tag{3.9}$$

denotes the normalized pth moment of the lattice.

Provided that the effective dimensionality of the source distribution $d > 8/\pi^2 \approx 0.81$, the quadratic approximation always implies a larger fraction of signals lost than the spherical ansatz, because $1 - \cos^d(r) < r^2 d/2$ on the interval $r \in [0, \pi/2]$.

Appendix A shows how the even moments may be computed for the $\mathbb{Z}^n$ lattice. The first six of these, which suffice for this paper, are

[2]We recall that in the x_i's coordinates the quadratic approximation to the mismatch is $m \approx r^2 = \Delta x_1^2 + \cdots + \Delta x_n^2$.

$$\langle r^2\rangle = \frac{n\ell^2}{12},$$
$$\langle r^4\rangle = \frac{n\ell^4}{720}(5n+4),$$
$$\langle r^6\rangle = \frac{n\ell^6}{60480}(35n^2+84n+16),$$
$$\langle r^8\rangle = \frac{n\ell^8}{3628800}(175n^3+840n^2+656n-96),$$
$$\langle r^{10}\rangle = \frac{n\ell^{10}}{95800320}(385n^4+3080n^3+5456n^2+352n-768),$$
$$\langle r^{12}\rangle = \frac{n\ell^{12}}{523069747200}(175175n^5+2102100n^4 +6646640n^3+3747744n^2-2883712n+35328). \tag{3.10}$$

We note that all of these quantities can be expressed in terms of the covering radius $R^2 = n\ell^2/4$. The corresponding even moments for the A_n^* lattice are computed in Appendix B, but not repeated here.

In the following we shall consider $d = 2$- and $d =$ 3-dimensional source distributions.

A. The $\mathbb{Z}^n$ lattice: $d = 2$ case

For a source distribution with effective dimensionality $d = 2$, we now evaluate the fraction of lost sources, assuming that the covering radius $R \le \pi/2$. The integrand of Eq. (3.8) ($f(r) = \sin^2 r$, the mismatch in the spherical ansatz [27]) is approximated (within 1%) by taking terms up to the eighth moment. Then, Eq. (3.8) takes the form

$$\frac{N_{\rm lost}}{N_D} \approx \langle r^2\rangle - \frac{1}{3}\langle r^4\rangle + \frac{2}{45}\langle r^6\rangle - \frac{1}{315}\langle r^8\rangle = \frac{1}{3}R^2 - \frac{5n+4}{135n}R^4 + \frac{70n^2+168n+32}{42525n^2}R^6 - \frac{175n^3+840n^2+656n-96}{4465125n^3}R^8. \tag{3.11}$$

We plot this quantity in Fig. 2(a), where $m_{\rm worst} = \sin^2 R$ denotes the worst-case mismatch in the spherical ansatz.

Figure 2(a) also compares the spherical ansatz [27] to the mismatch with the prediction one would find using the normal quadratic approximation. If the lattice is widely spaced (sparse), then the spherical ansatz predicts significantly fewer lost signals than the standard quadratic approximation. The quadratic approximation keeps only the first term in Eq. (3.11), so

$$\left[\frac{N_{\rm lost}}{N_D}\right]_{\text{Quadratic approximation}} = \frac{1}{3}\arcsin^2(\sqrt{m_{\rm worst}}), \tag{3.12}$$

which is valid in any dimension n.

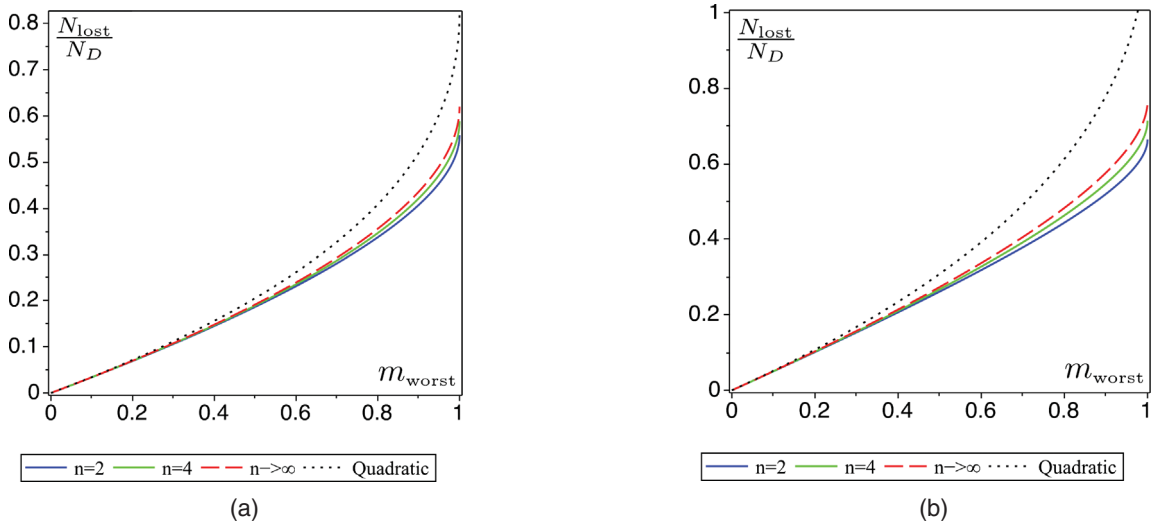

FIG. 2. The fraction of lost detections for the $\mathbb{Z}^n$ lattice in dimensions $n = 2$ (lower solid curve) and $n = 4$ (upper solid curve). For larger n the corresponding curves group very close together; the red dashed curve shows the $n \to \infty$ limit of Eq. (4.1). The left-hand plot shows a $d = 2$-dimensional source distribution and the right-hand plot shows a $d = 3$-dimensional distribution. The fraction of lost detections depends upon the spacing of the template bank, which is set by the covering radius R; with the spherical ansatz [27], the worst mismatch $m_{\rm worst} = \sin^2 R$. For closely spaced templates (small R) no detections are lost. For comparison the quadratic approximation Eq. (3.12) is shown as a dotted curve. It predicts more lost signals than the spherical ansatz suggests. The fraction of lost detections at maximum mismatch $R = \pi/2$ is given in Table I. As $n \to \infty$ and at covering radius $R = \pi/2$, about 62% of detections are lost for a $d = 2$-dimensional source distribution, and about 77% are lost for a $d = 3$-dimensional source distribution.

TABLE I. The maximal fraction of lost detections $N_{\rm lost}/N_D$ for the $\mathbb{Z}^n$ and A_n^* lattices in small dimensions n, for $d=2$- and $d=3$-dimensional source distributions. Note that all lattices have "maximal" WS radius $R=\pi/2$, which means that at a fixed dimension n, the WS cells have smaller volume for $\mathbb{Z}^n$ than for A_n^*.

	$\mathbb{Z}^n$	$\mathbb{Z}^n$	A_n^*	A_n^*
n	$d=2$	$d=3$	$d=2$	$d=3$
2	0.558	0.665	0.642	0.736
3	0.579	0.697	0.720	0.816
4	0.589	0.714	0.771	0.863
5	0.595	0.724	0.806	0.893
6	0.599	0.731	0.832	0.914
7	0.602	0.736	0.851	0.928
8	0.605	0.740	0.867	0.939
9	0.606	0.743	0.880	0.948
10	0.608	0.745	0.890	0.954
11	0.609	0.747	0.899	0.960
12	0.610	0.749	0.906	0.964
$n\to\infty$	0.620	0.766	1	1

To make a fair comparison of the spherical ansatz and the quadratic approximation, we need to examine Eq. (3.11) and Eq. (3.12) for the same lattice, with the same spacing, implying identical WS radius R. In this case, Eq. (3.12) gives the worst-case mismatch via the spherical ansatz [27] $m_{\rm worst}=\sin^2 R$ (rather than via the quadratic approximation $m_{\rm worst}=R^2$). In what follows, we carry out this fair comparison for the $\mathbb{Z}^n$ lattice in $d=3$ case and for the A_n^* lattice in $d=2$ and $d=3$ cases.

Results of numerical computations of the maximal fraction of lost detections are presented in Table I.

B. The $\mathbb{Z}^n$ lattice: $d=3$ case

For $d=3$ the integrand in Eq. (3.8) is $f(r)=1-\cos^3 r$, and we again assume $R\le\pi/2$. The expression Eq. (3.8) takes the following form:

$$\frac{N_{\rm lost}}{N_D}\approx\frac{3}{2}\langle r^2\rangle-\frac{7}{8}\langle r^4\rangle+\frac{61}{240}\langle r^6\rangle-\frac{547}{13440}\langle r^8\rangle+\frac{703}{172800}\langle r^{10}\rangle-\frac{44287}{159667200}\langle r^{12}\rangle. \tag{3.13}$$

Here, to maintain 1% accuracy in the integrand we have had to include more terms than for $d=2$. Figure 2(b) illustrates how the fraction of lost detections depends on the covering radius (via the worst-case mismatch $m_{\rm worst}$). In the case of quadratic approximation we keep only the first term in Eq. (3.13),

$$\left[\frac{N_{\rm lost}}{N_D}\right]_{\text{Quadratic approximation}}=\frac{1}{2}\arcsin^2(\sqrt{m_{\rm worst}}), \tag{3.14}$$

valid in any dimension n. For a widely spaced lattice the spherical ansatz predicts significantly fewer lost signals than the standard quadratic approximation. The worst-case values (fraction of lost detections at WS radius $R=\pi/2$) are shown in Table I.

C. The A_n^* lattice: $d=2$ and $d=3$ cases

As for the $\mathbb{Z}^n$ lattice, we can again estimate how the fraction of lost detections depends upon the covering radius. For the A_n^* lattice, we can compute the moments $\langle r^p\rangle$ exactly, but cannot give a closed analytic form as we did for the $\mathbb{Z}^n$ lattice. We use the exact expressions obtained in Appendix B, and substitute these into the expressions Eq. (3.11) and Eq. (3.13). The plots of the fraction of lost detections versus $m_{\rm worst}$ are given in Fig. 3, and some worst-case values are shown in Table I.

IV. LARGE-n LIMITS

The reader will notice that as the dimension n of the parameter space gets large, the curves appear to approach a limit. This is explained in Sec. VI, where we show that as n gets large, the mismatch distribution function becomes sharply peaked at $r^2=R^2/3$ for the $\mathbb{Z}^n$ lattice and at $r^2=R^2$ for the A_n^* lattice. Thus, for the $\mathbb{Z}^n$ lattice, Eq. (3.8) immediately gives

$$\lim_{n\to\infty}\frac{N_{\rm lost}}{N_D}=1-\cos^d(R/\sqrt{3})=1-\cos^d\left(\frac{\arcsin\sqrt{m_{\rm worst}}}{\sqrt{3}}\right), \tag{4.1}$$

where we have used the relationship $m_{\rm worst}=\sin^2 R$ between the WS radius and the worst-case mismatch.

For a source distribution with effective dimensionality $d=2$ this has a limiting value of $N_{\rm lost}/N_D\approx 0.620$ for $m_{\rm worst}=1$. So, if there are at least a few dimensions to parameter space, then placing templates in a rectangular grid at unit mismatch will recover about 38% of signals. For a source distribution with effective dimensionality $d=3$, the limiting value is $N_{\rm lost}/N_D\approx 0.766$, so a rectangular grid at unit mismatch would recover about 23% of signals.

In the case of the A_n^* lattice, Sec. VI shows that in the limit of large n we have

$$\lim_{n\to\infty}\langle r^2\rangle_{\rm WS}=R^2, \tag{4.2}$$

where the covering radius $R\in(0,\pi/2]$. In fact this is also true for the higher moments, as can be seen from either Sec. VI or from the results of Appendix B, meaning that

$$\lim_{n\to\infty}\langle r^{2m}\rangle_{\rm WS}=R^{2m},\quad m=1,2,3,\ldots. \tag{4.3}$$

Thus,

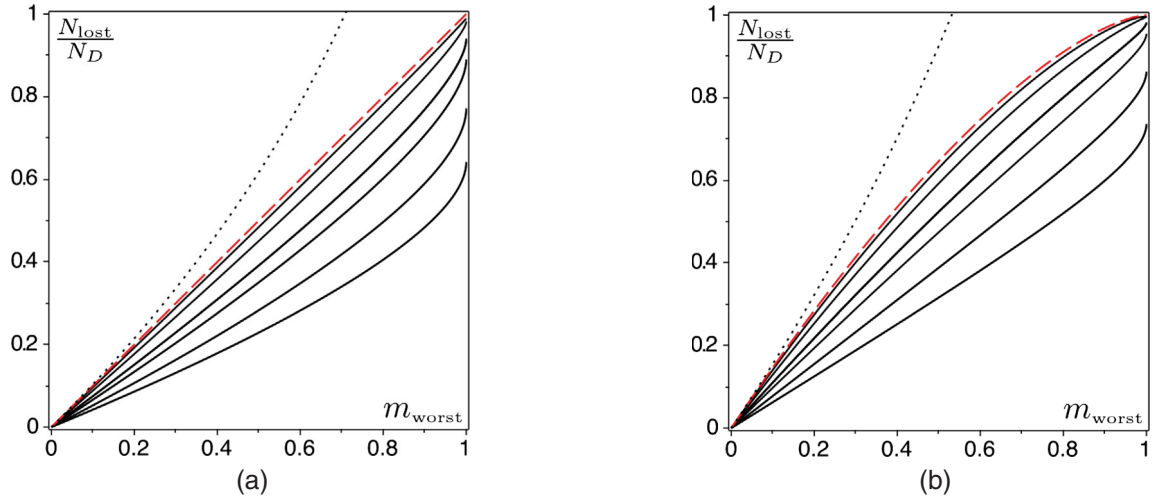

FIG. 3. The fraction of lost detections for the A_n^* lattice in different numbers of dimensions (moving upwards) $n = 2, 4, 10, 20, 100, 1000$. The left-hand plot shows a $d = 2$-dimensional source distribution and the right-hand plots shows a $d = 3$-dimensional distribution. As in the previous figure, the $n \to \infty$ limit is shown in red, and the plot is restricted to $R \le \pi/2$. The quadratic approximation is shown as a dotted curve in the limit $n \to \infty$ [see Eq. (4.5)]. The fraction of lost detections at maximum mismatch $R = \pi/2$ is given in Table I.

$$\lim_{n\to\infty} \frac{N_{\rm lost}}{N_D} = 1 - \cos^d R, \tag{4.4}$$

which leads to a worst-case limit of unity, as shown in Table I. For large dimensions the quadratic approximation of the fraction of lost detections can also be constructed in the closed form [cf. Eq. (3.12)],

$$\lim_{n\to\infty} \left[\frac{N_{\rm lost}}{N_D}\right]_{\text{Quadratic approximation}} = \frac{d}{2}\arcsin^2(\sqrt{m_{\rm worst}}). \tag{4.5}$$

This expression is shown by the dotted curves in Fig. 3.

V. COMPARISON OF $\mathbb{Z}^n$ AND A_n^* AT FIXED NUMBER OF TEMPLATES

To evaluate the relative loss fractions of the $\mathbb{Z}^n$ and A_n^* lattices at fixed number of templates, we must compare them for identical values of the WS cell volume $V_{\rm WS}$. This ensures that the same number of templates would be employed to cover a given volume of parameter space.

Such a comparison is shown in Fig. 4. The horizontal axis "x" in these plots is proportional to the "squared length" $V_{\rm WS}^{2/n}$. In the figure, this is normalized to reach unity when the covering radius of the A_n^* lattice reaches $R = \pi/2$. From Eq. (2.21), the resulting normalization factor is the inverse of

$$V_{\text{WS-Max}}^{2/n} = [V_{\rm WS}^{A_n^*}(R = \pi/2)]^{2/n} = \frac{3\pi^2(n+1)}{n(n+2)}(n+1)^{-1/n}. \tag{5.1}$$

Thus, if we denote the horizontal axes of Fig. 4 by $x = (V_{\rm WS}/V_{\text{WS-Max}})^{2/n}$, by using Eq. (2.9) and Eq. (2.21) we have

$$x = \begin{cases} \frac{4}{3\pi^2}\left(\frac{n+2}{n+1}\right)(1+n)^{1/n}R^2 & \text{for } \mathbb{Z}^n \\ \frac{4R^2}{\pi^2} & \text{for } A_n^*, \end{cases} \tag{5.2}$$

where R is WS cell covering radius of the corresponding lattice. Note that when the two lattices are compared at a given point on the x axis, they have equal WS cell volume; hence, they have *different* WS radii, and correspondingly *different* values of ℓ.

At fixed $V_{\rm WS}$, the WS radius R of the $\mathbb{Z}^n$ lattice is always larger than the WS radius of the A_n^* lattice. Since we allow the WS radius for A_n^* to reach maximal value $\pi/2$, it follows that in the plots in Fig. 4, the WS radius of $\mathbb{Z}^n$ exceeds $\pi/2$ for some of the domain. The transition point where the WS radius of $\mathbb{Z}^n$ reaches $R = \pi/2$ is denoted by a dot on the curves; to the right of this dot, the mismatch of the $\mathbb{Z}^n$ lattice is set to unity for $r > \pi/2$ in accordance with Eq. (3.7). Thus, to the right of this dot, the $\mathbb{Z}^n$ results have been obtained with Monte Carlo integration, since the analytic formulas obtained earlier only hold for $R \le \pi/2$. As can be seen from Eq. (5.2), the location of this dot approaches $x = 1/3$ in the large-n limit.

One can see that these plots have taken us away from the quadratic approximation to the mismatch. To get some sense of how far away, consider the maximum mismatch at the locations of the dots. In the quadratic approximation, this would be $m = r^2 = \pi^2/4 \approx 2.47$, more than double the maximum allowed value of $m = 1$. In the quadratic approximation to the mismatch, the lower curves of Fig. 4

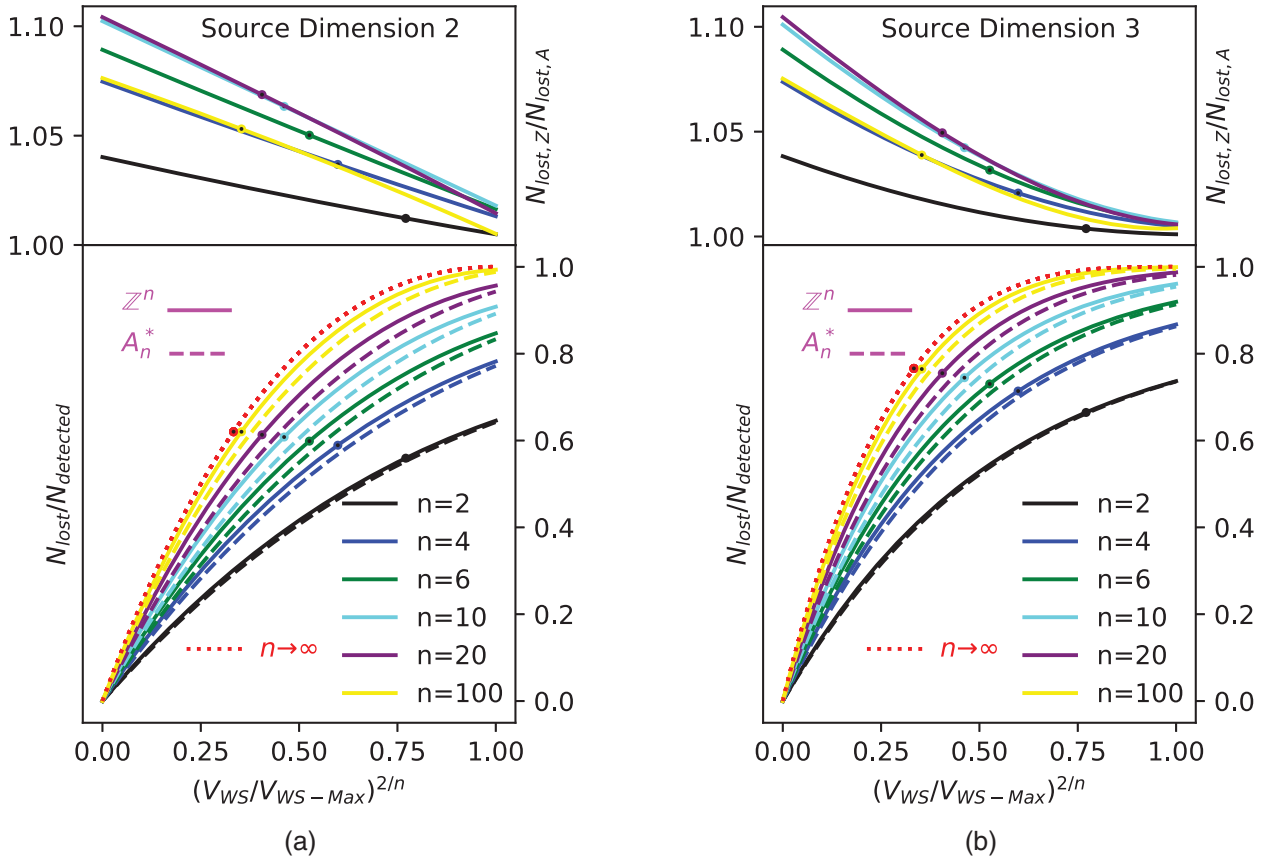

FIG. 4. A comparison of lattice loss fractions at fixed number of templates. Lower curves: the loss fractions $N_{\rm lost}/N_D$ for the $\mathbb{Z}^n$ and A_n^* lattices, at fixed WS cell volume $V_{\rm WS}$. The red dotted curves represent the lattice loss fraction in the limit $n \to \infty$ [see Eq. (5.3)]. Upper curves: ratios of these loss fractions. The horizontal axis normalization is given by Eq. (5.1). The dots on the curves indicate where the covering radius for $\mathbb{Z}^n$ reaches $R = \pi/2$. The left (right) plots are for a $d = 2$ ($d = 3$)-dimensional source distributions.

would be straight lines tangent to the given curves at $V_{\rm WS} = 0$. The upper curves would be horizontal lines passing through the $V_{\rm WS} = 0$ values.

The results of [25] show that for small mismatch, where the quadratic approximation applies, the A_n^* lattice is only slightly less lossy than the $\mathbb{Z}^n$ lattice. We can now see that this marginal advantage *decreases* for larger mismatch: the upper part of Fig. 4 shows the ratio of the loss fractions for the two lattices. The efficiency of the A_n^* lattice is at most $\approx$10% higher than that of the $\mathbb{Z}^n$ lattice.

The large-n limits of Sec. IV are informative and can be easily evaluated. Taking $n \to \infty$ in Eq. (5.2) the loss fractions Eq. (4.1) and Eq. (4.4) for both the lattices take the identical form:

$$\frac{N_{\rm lost}}{N_D} = 1 - \cos^d\left(\frac{\pi}{2}\sqrt{x}\right). \tag{5.3}$$

This is shown by the dotted red curves in Fig. 4. The transition point $x = 1/3$ is indicated with a dot; at that point the covering radius of the $\mathbb{Z}^n$ lattice is equal to $\pi/2$. While the A_n^* lattice has the same curve, the transition is only relevant for the $\mathbb{Z}^n$ lattice. For large n, the ratio of the loss fractions approaches unity, as can be seen from Eq. (5.3).

VI. DISTRIBUTION FUNCTION OF THE SQUARED DISTANCE

To understand and interpret the results presented above, it is helpful to define the *mismatch distribution function* $P_m(m)$. This is a probability distribution: if points in parameter space are chosen "at random," then the probability that the mismatch lies in the range $(m, m + dm)$ is $P_m(m)dm$. Here, we compute $P_m(m)$ under the assumption that the probability of selecting a particular point in parameter space is a uniform distribution in the lattice coordinates $y_i \in [0, \ell]$. This is equivalent to a uniform distribution in x_i.

With the quadratic approximation and the spherical ansatz [27], the mismatch is a one-to-one function of the squared distance r^2, assuming of course in the spherical case that we restrict attention to $r \in [0, \pi/2]$. Hence, the mismatch distribution can be obtained from the radius distribution function $P_{r^2}(r^2)$, assuming the same uniform distribution of

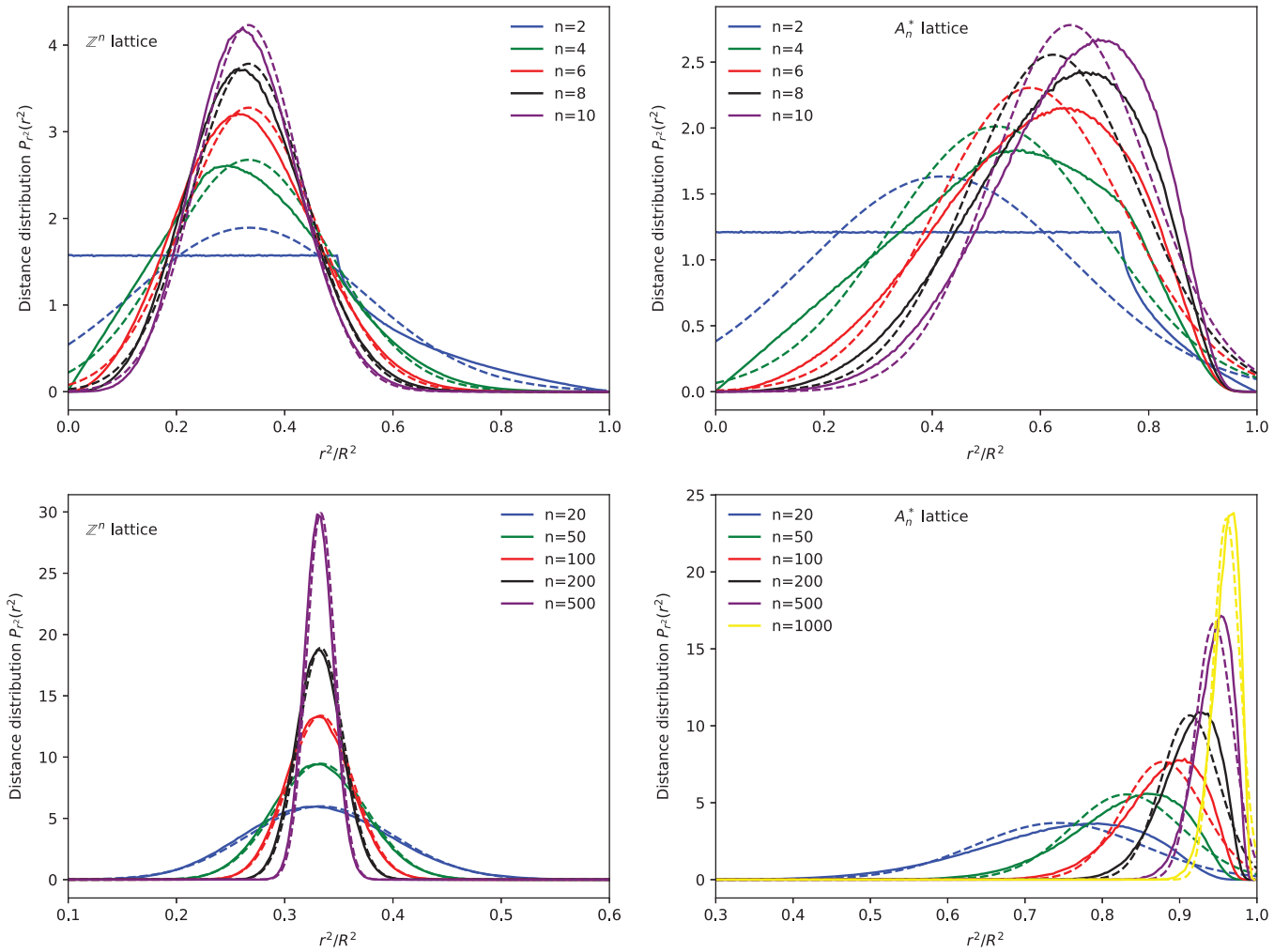

FIG. 5. The probability distribution of the squared distance $P_{r^2}(r^2)$ is shown as the solid curves for the $\mathbb{Z}^n$ (left plots) and A_n^* (right plots) lattices, for a varying number of dimensions n. The top curves show small dimensions $n = 2, 4, 6, 8, 10$ and the lower curves show larger dimensions $n = 20, 50, 100, 200, 500$. The dotted curves show the Gaussian approximation given in Eq. (6.4), with the correct mean and variance for the given lattice and dimension. One can see that for the $\mathbb{Z}^n$ lattice, as expected from the central limit theorem, the Gaussian approximation approaches the true distribution as $n \to \infty$, which is a Dirac delta function peaked at $r^2/R^2 = 1/3$. For A_n^*, the central limit theorem does not apply, and the Gaussian approximation does not approach the true distribution for large dimension. Nevertheless, as $n \to \infty$, the distributions approaches a Dirac delta function peaked at $r^2/R^2 = 1$. Similar plots are presented in [17].

the y_i. This distribution function can be used to compute an average value of an integrable function f of r^2,

$$\langle f(r^2)\rangle = \frac{1}{V_{\rm ws}}\int_{\rm ws} f(r^2)dV = \int_0^{R^2} f(r^2)P_{r^2}(r^2)dr^2. \tag{6.1}$$

Thus, the quantity we wish to compute is the distribution of the values of the quadratic forms given in Eq. (2.5) for the $\mathbb{Z}^n$ lattice and in Eq. (2.11) for the A_n^* lattice.

A. r^2 distribution for the $\mathbb{Z}^n$ lattice

For finite values of the dimension n we have not found a simple closed form for $P_{r^2}(r^2)$, although we can give expressions for $n = 1$, 2, and 3. However, the large-n limit is easily computed.

To compute the radius distribution function $P_{r^2}(r^2)$ for large n, we make use of the central limit theorem [35]. Consider the distance Eq. (2.5). In the large-n limit it is the sum of many independent random variables, each of which has the same distribution. Thus, we expect that it should approach a normal or Gaussian distribution, characterized entirely by the mean and variance of the distribution.

We have already calculated the moments of r^2 for the $\mathbb{Z}^n$ lattice in Eq. (3.10). The mean and variance are given by

$$\langle r^2\rangle = \frac{1}{12}n\ell^2 = \frac{1}{3}R^2, \tag{6.2}$$

and

$$\sigma^2 = \langle r^4\rangle - \langle r^2\rangle^2 = \frac{1}{180} n\ell^4 = \frac{4}{45n} R^4. \qquad (6.3)$$

From these, the large-n limit follows immediately. Note that as n gets large, the variance vanishes, which means that the distribution becomes sharply peaked.

If n is large enough that the central limit theorem applies, then the distribution of squared distance approaches a Gaussian normal distribution:

$$P_{r^2}(r^2)dr^2 = (2\pi\sigma^2)^{-1/2} e^{-(r^2-R^2/3)^2/2\sigma^2} dr^2. \qquad (6.4)$$

Note that if the dimension n is large, then this has vanishing support for negative r^2, otherwise the normalization may be suitably adjusted.

In the $n \to \infty$ limit with fixed mismatch, the variance vanishes, and the distribution approaches a Dirac delta function

$$\lim_{n\to\infty} P_{r^2}(r^2) = \delta\left(r^2 - \frac{1}{3}R^2\right). \qquad (6.5)$$

In Fig. 5 we show how this limit is approached. When n is larger than 2, one has $2\sigma^2 < (R^2/3)^2$ and as soon as n is a few times larger than this, the Gaussian distribution becomes a good approximation to the actual mismatch.

B. r^2 distribution for the A_n^* lattice

The case of the A_n^* lattice is not as simple. The squared distance is still a quadratic form which can be diagonalized, but the variables which make it up are no longer independent, because they are constrained by the boundaries of the WS. It is unlike the $\mathbb{Z}^n$ lattice, where these constraints are independent for each variable. Hence, the central limit theorem cannot be applied.

It is informative to examine the moments of r^2 defined by Eq. (3.9), which are computed exactly via recursion in Appendix B. Figure 6 shows the mean and variance of r^2 for the A_n^* lattice. One immediately sees a significant difference when compared with the $\mathbb{Z}^n$ lattice: at large dimension, the mean value of squared radius $\langle r^2\rangle$ approaches the squared WS radius R^2, whereas for $\mathbb{Z}^n$ it is $1/3$ of that value. As with the cubic lattice, the variance approaches zero at large dimension, indicating that the distribution is becoming sharply peaked. Some higher moments $\langle r^{2m}\rangle$ are shown in Fig. 7: for large n they asymptote to R^{2m}.

It is straightforward to study the distribution function numerically. First, select points at random from within the FP, by drawing the lattice coordinates $y_1, \ldots, y_n$ from independent uniform distribution in the range $[0, \ell]$. Then identify the closest lattice point to $x = y_i \boldsymbol{e}_i$ and calculate the distance between the two. We now describe how to identify this closest lattice point. (An algorithm is given in [29] for A_n as well as the correspondence with the dual lattice A_n^*, but we were unable to implement it.)

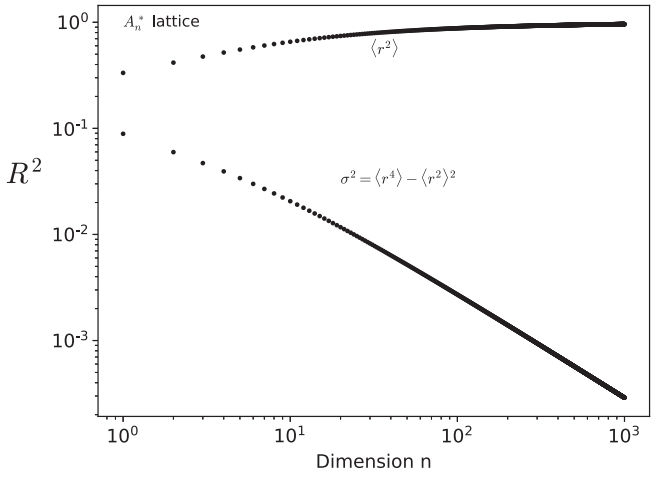

FIG. 6. The mean and variance of the squared radius for the A_n^* lattice for dimensions from 1 to 1000, obtained exactly using the recursion in Appendix B. At large dimension the distribution is a narrow peak at the squared WS radius R^2.

It is straightforward to show that the closest lattice point to x must be one of the vertices of the FP. Since there are 2^n such vertices, when n is large, it is not computationally feasible to check the distances to all of them. However, it is trivial to show that the distance to the closest lattice point is unchanged if we permute the ordering of the lattice coordinates y_i. So the first step of simplification is to reorder the lattice coordinate values of y_i in increasing order.

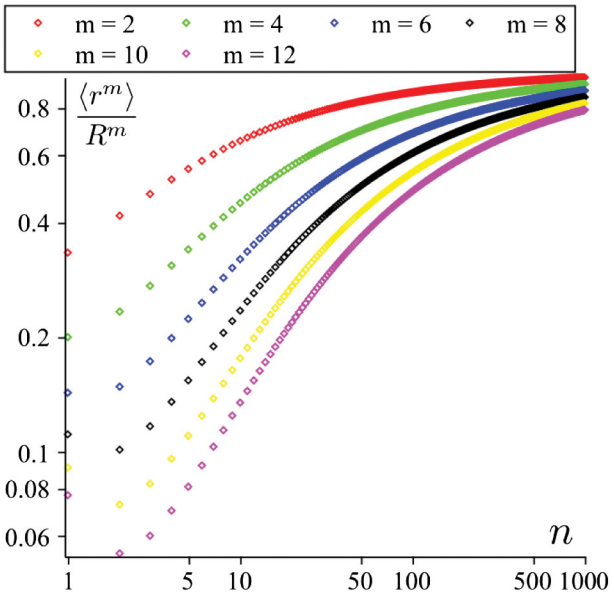

FIG. 7. The even moments $\langle r^m\rangle$ for $m = 2, 4, 6, 8, 10, 12$ in the units of R^m for the A_n^* lattice for dimensions from 1 to 1000 are shown in the ascending order.

We now prove the following. If $0 \le y_1 \le \cdots \le y_n \le \ell$ are the lattice coordinates of a point in the FP, then the closest FP vertex has coordinates of the form $(0, \ldots, 0, \ell, \ldots, \ell)$, where there are k zeros followed by $(n-k)$ ℓ's. The proof is by contradiction.

Suppose that the closest vertex to the point with lattice coordinates $(y_1, \ldots, y_n)$ is a point with lattice coordinates $A = (0, \ldots, 0, \ell, 0, \ell, \ldots, \ell)$ and is at squared distance r_A^2. We use y_R to denote the lattice coordinate value at the position of the rightmost zero, and y_L to denote the value at the leftmost ℓ. Now, construct a different lattice vertex B, by swapping the leftmost ℓ with the 0 just to its right, so that $B = (0, \ldots, 0, \ell, \ell, \ldots, \ell)$, and denote its squared distance from y by r_B^2. The difference between the squared distances is

$$\begin{aligned} r_A^2 - r_B^2 &= \left(1 + \frac{1}{n}\right)((y_L - \ell)^2 + y_R^2 - (y_R - \ell)^2 - y_L^2)) \\ &= 2\ell\left(1 + \frac{1}{n}\right)(y_R - y_L). \end{aligned} \tag{6.6}$$

Since the coordinates are ordered so that $y_L < y_R$, it follows that $r_A^2 - r_B^2 > 0$ and thus that A is *not* the closest lattice vertex to y. The same argument shows that swapping a leftmost ℓ with a 0 anywhere to its right will always decrease the distance. The result follows by induction.

This makes it computationally straightforward to identify the closest vertex to any point inside the FP. First, sort the lattice coordinates in increasing order. Then, calculate the distances to the $n+1$ vertices with coordinates of the form $(0, \ldots, 0, \ell, \ldots, \ell)$ and select the minimum.

We have used this method to find $P_{r^2}(r^2)$ numerically for the A_n^* lattice, for dimensions from $n = 1$ to $n = 1000$. This is plotted in Fig. 5. In comparison with the cubic lattice $\mathbb{Z}^n$, two differences are immediately apparent. The first is that as the dimension n increases, the distribution increasingly becomes peaked around the WS radius R, and the second is that the Gaussian approximation (with the correct mean and variance) is not good, because it does not fall off fast enough as $r \to R$.

VII. CONCLUSION

In this paper, we have computed and compared the loss fractions of two template grids. The first is based on the simple cubic lattice $\mathbb{Z}^n$, and the second is based on the root lattice A_n^*, which is a generalization of the two-dimensional hexagonal lattice. In particular, we extend the results of [25] to the case of large mismatch, by exploiting the spherical ansatz [27].

The main result is rather clear, and visible in the plots in the upper parts of Fig. 4. The slight advantages offered by the A_n^* lattice at small mismatch *decrease* at larger mismatch. This can be easily understood from the distribution of the squared radius for points randomly selected within a WS cell. As the dimension n of parameter space increases, this distribution becomes an increasingly narrow peak centered closer and closer to the squared WS radius. This behavior can be seen in the rhs plots of Fig. 5.

We believe that in the limit as the dimension $n \to \infty$, this may be the case for any lattice. To state it precisely, the distribution function for the squared radius becomes an increasingly narrow peak, which is true if and only if

$$\lim_{n\to\infty} \langle r^{2m} \rangle = \langle r^2 \rangle^m, \tag{7.1}$$

with the understanding that the WS radius R is held fixed during the limiting process. We have tried to prove this using Jensen's inequality [36], but are not convinced that our argument is correct.

One of the motivations for this work was the hope that replacing the $\mathbb{Z}^n$ lattices used in current continuous gravitational-wave and gamma-ray pulsar searches by "better" ones such as A_n^* would significantly increase the number of sources found. Unfortunately, the gain would be very small.

The results obtained in this paper are for two specific template banks, both constructed as regular lattices. However, we expect that these are representative of the behavior of all (generic) template banks, as the template spacings are increased beyond the quadratic approximation. Thus, they provide useful insights for the general case.

We conclude with two final messages for the data analyst:

First, a fairly effective template-based search can be constructed at mismatch values that are shockingly high in the quadratic approximation (quadratic mismatch exceeding unity!). For example, consider a four-dimensional parameter space and a two-dimensional source distribution (e.g., a search for isolated pulsars in a "planar" Galaxy). Place the templates on a $\mathbb{Z}^4$ lattice, spaced so that the quadratic approximation predicts a worst-case mismatch of 1. Then, according to the left-hand plot of Fig. 2, only $\approx$28% of signals[3] would be lost from the mismatch between signal and template parameters.

Second, if the goal is to detect as many signals as possible with a fixed number of templates, there is little incentive to build template banks with sophisticated lattices such as A_n^* instead of the humble cubic lattice $\mathbb{Z}^n$. While there may be particular cases where the small gains (typically less than 10%) are worth the trouble, for most purposes the effort is better invested elsewhere.

ACKNOWLEDGMENTS

We thank Mathieu Dutour Sikirić for bringing the thinnest known lattices of [31] to our attention and Reinhard Prix for careful reading of our paper and many useful suggestions.

[3]For $d = 2, n = 4$; $R^2 = 1$ implies that $m_{\text{worst}} = \sin^2 R \approx 0.708$.

APPENDIX A: EVEN MOMENTS OF THE $\mathbb{Z}^n$ LATTICE

For the $\mathbb{Z}^n$ lattice, the general even-order moment can be computed as follows. One uses the multinomial expansion to write

$$\langle r^{2m}\rangle = \sum_{k_1+\cdots+k_n=m} \binom{m}{k_1,\ldots,k_n} \prod_{i=1}^{n} \langle x_i^{2k_i}\rangle, \quad \text{(A1)}$$

where the sum is over all non-negative integer k_i's whose sum equals m. The multinomial coefficient is

$$\binom{m}{k_1,k_2,\ldots,k_n} = \frac{m!}{k_1!k_2!\cdots k_n!}, \quad \text{(A2)}$$

and the coordinate moments are

$$\langle x^{2k}\rangle = \frac{1}{\ell}\int_{-\ell/2}^{\ell/2} x^{2k}dx = \frac{1}{2k+1}\left(\frac{\ell}{2}\right)^{2k}. \quad \text{(A3)}$$

In the sum Eq. (A1), there are many identical terms on the rhs which are obtained by permutation of the indices of the k_i. The number of these identical terms depends upon the number of distinct nonzero values taken by the k_i, which in turn depends upon the dimension n.

Suppose that for each term, the nonzero k_i are sorted in increasing order; there are at most m of them. Let $q \le m$ denote the number of these nonzero k_i, and let n_1 denote the number of k_i which have the smallest value, n_2 the next smallest, and so on; the sum is bounded by $\sum_i n_i \le m$. Then the number of equivalent (under permutation) terms which appear on the rhs of Eq. (A1) is equal to the number of ways in which n_1 coordinates can be chosen from the n, and n_2 can be chosen from the remaining $n-n_1$, and so on. This is

$$\begin{aligned} N(k_1,\ldots,k_q) &= \binom{n}{n_1}\binom{n-n_1}{n_2}\times\cdots\times\binom{n-n_1-\cdots-n_{p-1}}{n_p} \\ &= \frac{n!}{n_1!n_2!\cdots n_p!(n-n_1-\cdots-n_p)!}, \end{aligned} \quad \text{(A4)}$$

where the quantities in the second line are the standard binomial (choice) coefficients; the rhs is a polynomial in n of order $\le m$. Thus one obtains

$$\langle r^{2m}\rangle = \sum_{k_1+\cdots+k_q=m} \frac{\binom{m}{k_1,\ldots,k_q} N(k_1,\ldots,k_q)}{(2k_1+1)\cdots(2k_q+1)} \left(\frac{\ell}{2}\right)^{2m}, \quad \text{(A5)}$$

where the sum is over all distinct (under permutation) partitions k_i.

For example, for $m=5$, the rhs of Eq. (A5) has seven terms, with the following sets of k_i: $\{1,1,1,1,1\}$, $\{1,1,1,2\}$, $\{1,2,2\}$, $\{1,1,3\}$, $\{2,3\}$, $\{1,4\}$, and $\{5\}$. Respectively, these have n_i given by $\{5\},\{3,1\},\{1,2\}$, $\{2,1\},\{1,1\},\{1,1\}$, and $\{1\}$, with corresponding N given by $n(n-1)(n-2)(n-3)(n-4)/5!$, $n(n-1)(n-2)(n-3)/3!$, $n(n-1)(n-2)/2!$, $n(n-1)(n-2)/2!$, $n(n-1)$, $n(n-1)$ and n. Thus one obtains

$$\begin{aligned} \left(\frac{\ell}{2}\right)^{-10}\langle r^{10}\rangle = {} & \binom{5}{1,1,1,1,1}\frac{n(n-1)(n-2)(n-3)(n-4)}{5!3^5} + \binom{5}{1,1,1,2}\frac{n(n-1)(n-2)(n-3)}{3!3^35} \\ & + \binom{5}{1,2,2}\frac{n(n-1)(n-2)}{2!5^23} + \binom{5}{1,1,3}\frac{n(n-1)(n-2)}{2!3^27} \\ & + \binom{5}{2,3}\frac{n(n-1)}{5\cdot 7} + \binom{5}{1,4}\frac{n(n-1)}{3\cdot 9} + \binom{5}{5}\frac{n}{11}. \end{aligned}$$

This simplifies, to give the tenth moment of Eq. (3.10).

The supplementary material [37] for this manuscript include a short *Mathematica* script to calculate arbitrary even moments of the $\mathbb{Z}^n$ lattice.

APPENDIX B: EVEN MOMENTS OF THE A_n^* LATTICE

Here we give a general expression for computation of any even moment of the A_n^* lattice. The computation is a generalization of Chapter 21, Sec. 3.F of [29], where the second moment is found.

The un-normalized and normalized pth moments of a region or object D are defined as

$$U_p(D) = \int_D r^p dV, \text{ and } I_p(D) = U_p(D)/U_0(D), \quad \text{(B1)}$$

where D is the domain of integration and the radius r is measured from the origin O (see Fig. 8).

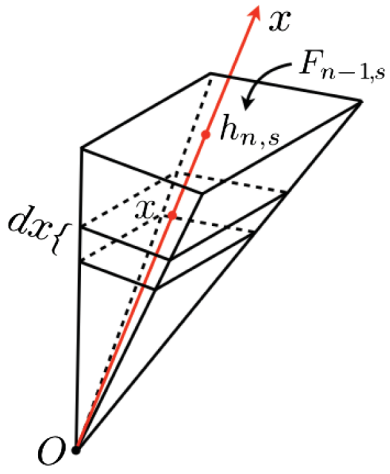

FIG. 8. The n-dimensional pyramid associated with $(n-1)$-dimensional face $F_{n-1,s}$. The point O is such that for all congruent faces $F_{n-1,s}$ the associated pyramids are congruent. The axis Ox is perpendicular to the face $F_{n-1,s}$, and $h_{n-1,s}$ is the distance form O to the face. The increment dx is thickness of the slab at x.

The WS cell in dimension n is called a permutohedron and is denoted P_n. It has a complex shape with $(n+1)!$ vertices and $2^{n+1}-2$ faces. According to the definition Eq. (B1), $U_0(P_n)$ is the volume of the WS cell P_n. The normalized mth moment $I_p(P_n)$ is obtained by dividing out the volume.

Note that the length conventions used in this Appendix follow [29], and differ from the conventions used in the remainder of this paper. To transform a quantity associated with P_n with dimensions of $(\text{length})^d$ in this section into the units used in the remainder of the paper, multiply by

$$\left[\frac{\ell^2}{n(n+1)}\right]^{d/2}. \tag{B2}$$

For example, in the conventions of this section, the point in P_n most distant from the center has squared radius $n(n+1)(n+2)/12$, which should be compared with Eq. (2.20), and the n-volume is $U_0(P_n)=(n+1)^{n-1/2}$, which should be compared with Eq. (2.14).

Each face of P_n is the direct product of a pair of lower-dimensional permutohedrons.[4] For n even there are $n/2$ types of faces and for n odd there are $(n+1)/2$ types of faces. Following [29] the different types of faces are labeled by $s=0,\ldots,n-1$. A face of type s, $F_{n-1,s}$, is the Cartesian product, $F_{n-1,s}=P_s\times P_{n-s-1}$; faces of type s and faces of type $n-s-1$ are equivalent. The number of faces of type s is the binomial coefficient

$$\binom{n+1}{s+1}. \tag{B3}$$

The squared distance from the center of P_n to the center of a face of type s is

$$h_{n,s}^2=\frac{1}{4}(s+1)(n-s)(n+1). \tag{B4}$$

By symmetry, the line from the center of P_n to the center of any face is orthogonal to the face. We call this the center line to the face.

Because the faces are formed from lower-dimensional permutohedrons, the moments may be calculated by recursion. We divide P_n into generalized pyramids, one face at a time, by taking the bundle of all line segments that begin at the center of the P_n and extend to anywhere in that face. These pyramids are disjoint (apart from a set of measure zero on their boundaries) and their union is P_n. To compute the moments of P_n, we compute the moments of the pyramids and sum them.

The mth moment of each pyramid can be found with elementary calculus. We slice each pyramid into slabs of thickness dx, where $x\in[0,h_{n,s}]$ is a a coordinate that runs along the center line to a face of type s, and the slicing is orthogonal to the center line shown in Fig. 8. Each slab has n-volume

$$dV=\frac{x^{n-1}}{h_{n,s}^{n-1}}U_0(P_s)U_0(P_{n-s-1})dx, \tag{B5}$$

so by integration over x the volume of the pyramid is

$$\int_0^{h_{n,s}}dV=\frac{1}{n}h_{n,s}U_0(P_s)U_0(P_{n-s-1}). \tag{B6}$$

Summing over all faces gives

$$U_0(P_n)=\frac{1}{n}\sum_{s=0}^{n-1}\binom{n+1}{s+1}h_{n,s}U_0(P_s)U_0(P_{n-s-1}). \tag{B7}$$

This recursion relation, together with the initial value $U_0(P_0)=1$, determines the volume $U_0(P_n)$ for dimensions $n>0$.

To construct a general recursion relation for an arbitrary even moment $U_{2m}(P_n)$, $m=0,1,2,3,\ldots$, we begin with the expression

$$U_{2m}(P_n)=\sum_{s=0}^{n-1}\binom{n+1}{s+1}U_{2m}(P_{n,s}), \tag{B8}$$

where $U_{2m}(P_{n,s})$'s are the moments of n-dimensional pyramids $P_{n,s}$ into which a permutohedron P_n is decomposed.

[4] A face of P_n is only the direct product (metrically as well as geometrically!) of lower-dimensional faces of P_n if we follow the "dimension-dependent" length conventions of [29].

TABLE II. Numerical values for the first six even moments of the WS cell P_n of the A_n^* lattice for dimensions $n = 1, \ldots, 15$, where the covering radius R is given in Eq. (2.20). The exact values of these moments are given in Table III. In the text we argue that $\lim_{n\to\infty}\langle r^2\rangle/R^2 = 1$, and that $\lim_{n\to\infty}\langle r^{2m}\rangle = \langle r^2\rangle^m$. Hence, as $n \to \infty$, all of these table entries should approach unity.

n	$\langle r^2\rangle/R^2$	$\langle r^4\rangle/R^4$	$\langle r^6\rangle/R^6$	$\langle r^8\rangle/R^8$	$\langle r^{10}\rangle/R^{10}$	$\langle r^{12}\rangle/R^{12}$
1	0.3333	0.2000	0.1429	0.1111	0.0909	0.0769
2	0.4167	0.2333	0.1482	0.1013	0.0727	0.0541
3	0.4750	0.2727	0.1728	0.1167	0.0824	0.0602
4	0.5187	0.3083	0.1987	0.1353	0.0959	0.0701
5	0.5529	0.3397	0.2233	0.1540	0.1101	0.0810
6	0.5807	0.3672	0.2460	0.1720	0.1242	0.0921
7	0.6038	0.3914	0.2669	0.1891	0.1380	0.1031
8	0.6234	0.4130	0.2862	0.2052	0.1512	0.1139
9	0.6404	0.4324	0.3039	0.2204	0.1639	0.1244
10	0.6552	0.4499	0.3202	0.2346	0.1760	0.1346
11	0.6683	0.4657	0.3354	0.2481	0.1876	0.1444
12	0.6800	0.4802	0.3496	0.2608	0.1986	0.1539
13	0.6905	0.4936	0.3628	0.2728	0.2092	0.1630
14	0.7001	0.5058	0.3751	0.2842	0.2193	0.1719
15	0.7088	0.5172	0.3867	0.2950	0.2290	0.1804

Every such moment can be calculated by using the definition Eq. (B1), substituting for r^2 the expression

$$r^2 = \frac{x^2}{h_{n,s}^2}\rho_{n-1,s}^2 + x^2. \tag{B9}$$

Here $\rho_{n-1,s}$ is the distance from the point of intersection of the axis Ox with the face $F_{n-1,s}$ to an arbitrary point of the face (see Fig. 8). It follows that

$$U_{2m}(P_{n,s}) = \int_{F_{n-1,s}} dV \int_0^{h_{n,s}} dx \left(\frac{x^2}{h_{n,s}^2}\rho_{n-1,s}^2 + x^2\right)^m = \sum_{k=0}^{m}\binom{m}{k}\int_{F_{n-1,s}} \rho_{n-1,s}^{2k} dV \int_0^{h_{n,s}} \frac{x^{2m+n-1}}{h_{n,s}^{n-1+2k}}\,dx,$$

where the volume element dV is in the face $F_{n-1,s}$. (For odd moments $m = k + 1/2$, where $k = 0, 1, 2, \ldots$ the finite sum in the expression above is replaced by an infinite series.) Using the definition Eq. (B1) for the moments $U_{2k}(F_{n-1,s})$ of faces $F_{n-1,s}$ (here, with origin at the center of the face) and integrating over x we obtain

$$U_{2m}(P_{n,s}) = \frac{h_{n,s}^{2(m-k)+1}}{n+2m}\sum_{k=0}^{m}\binom{m}{k}U_{2k}(F_{n-1,s}). \tag{B10}$$

Substituting this expression into Eq. (B8) we obtain

$$U_{2m}(P_n) = \frac{1}{n+2m}\sum_{s=0}^{n-1}\sum_{k=0}^{m}\binom{n+1}{s+1}\binom{m}{k} \times h_{n,s}^{2(m-k)+1}U_{2k}(F_{n-1,s}). \tag{B11}$$

The next step is to consider the face $F_{n-1,s}$ as the Cartesian product $P_s \times P_{n-s-1}$ and apply again the definition Eq. (B1) to the moments $U_{2k}(F_{n-1,s})$, with the origin at the center of the face. Replace r^2 with

$$\rho_{n-1,s}^2 = \rho_s^2 + \rho_{n-1-s}^2, \tag{B12}$$

TABLE III. Exact values of the lowest-order even moments for the A_n^* lattice, as given by the recursion relationship derived in Appendix B. Numerical values may be found in Table II.

n	$\langle r^2\rangle/R^2$	$\langle r^4\rangle/R^4$	$\langle r^6\rangle/R^6$	$\langle r^8\rangle/R^8$	$\langle r^{10}\rangle/R^{10}$	$\langle r^{12}\rangle/R^{12}$
1	$\frac{1}{3}$	$\frac{1}{5}$	$\frac{1}{7}$	$\frac{1}{9}$	$\frac{1}{11}$	$\frac{1}{13}$
2	$\frac{5}{12}$	$\frac{7}{30}$	$\frac{83}{560}$	$\frac{319}{3150}$	$\frac{403}{5544}$	$\frac{1517}{28028}$
3	$\frac{19}{40}$	$\frac{409}{1500}$	$\frac{27217}{157500}$	$\frac{38281}{328125}$	$\frac{1427333}{17325000}$	$\frac{539235971}{8957812500}$
4	$\frac{389}{750}$	$\frac{37}{120}$	$\frac{312953}{1575000}$	$\frac{15977293}{118125000}$	$\frac{41514229}{433125000}$	$\frac{10041681373}{143325000000}$
5	$\frac{209}{378}$	$\frac{22469}{66150}$	$\frac{1085536}{4862025}$	$\frac{131002604}{850854375}$	$\frac{43271601607}{393094721250}$	$\frac{120676030448681}{1490484151406250}$
6	$\frac{78077}{134456}$	$\frac{423151}{1152480}$	$\frac{66683227}{271063296}$	$\frac{2855332489}{16602626880}$	$\frac{3049146605765}{24545323579392}$	$\frac{561024599680723}{6091703033794560}$
7	$\frac{89035}{147456}$	$\frac{1515163}{3870720}$	$\frac{3645004793}{13655900160}$	$\frac{813284979379}{4301608550400}$	$\frac{43871720179117}{317974904045568}$	$\frac{47003442367289761}{455737531223310336}$
8	$\frac{3313213}{5314410}$	$\frac{146336671}{354294000}$	$\frac{127738979843}{446410440000}$	$\frac{23552471440009}{114791256000000}$	$\frac{343658283760349}{2272866868800000}$	$\frac{265121318177296915 33}{2326847456934000000 0}$
9	$\frac{1100657}{1718750}$	$\frac{117719}{272250}$	$\frac{895784540747}{2947957031250}$	$\frac{535892016104111}{2432064550781250}$	$\frac{217007542831819286}{1324259147900390625}$	$\frac{742285895491560612 2659}{5965125331717309570 3125}$
10	$\frac{18539106101}{28295372292}$	$\frac{9643229133}{21435888100}$	$\frac{396436661186}{1237922537775}$	$\frac{7667873302060633}{32681154997260000}$	$\frac{5567291102721634 49}{3163535803734768000}$	$\frac{4395579391379571244226791}{3265658693899080979500 0000}$
11	$\frac{25941989}{38817792}$	$\frac{6463162733}{13877360640}$	$\frac{1863816574691}{5556495200256}$	$\frac{1400046042361}{5643315437760}$	$\frac{1406514743813641321}{7499234843102306304}$	$\frac{2642524744951527437 8841}{1829766431499193348 76160}$
12	$\frac{17061288862565}{25090245516518}$	$\frac{389281868476643}{810607932072120}$	$\frac{135373127776116799}{387267939547455330}$	$\frac{3186173305108287135529}{1221701259590390810400}$	$\frac{1943079236630533404123 17}{9783383689751984960968 32}$	$\frac{4484014556806441492657 3819}{2913669542511591157466 56512}$
13	$\frac{81923134171}{118639604580}$	$\frac{2718612928907}{5508267355500}$	$\frac{4772968402612073}{13157873645450625}$	$\frac{26384102217284296859}{96710371294062093750}$	$\frac{8775008810370829285906}{4194973538832100086 5625}$	$\frac{3034165287365868825626600411}{1860995136164390400901 2890625}$
14	$\frac{3588341852791}{5125781250000}$	$\frac{5807913344549}{11481750000000}$	$\frac{6330843027118853801}{16878172500000000000}$	$\frac{3357739197420742084967}{1181472075000000000000}$	$\frac{9575820529342227197910377}{4366720789200000000000000}$	$\frac{1738380116833219461959 4087887}{1011491324625600000000000000}$
15	$\frac{423929152911307}{598134325510144}$	$\frac{49305729309609649}{95327658128179200}$	$\frac{2105510886390505559 33}{5445115832281595904 00}$	$\frac{1950534221728137033 5341}{6611926367770509312 0000}$	$\frac{2717862892853853098 16213443}{1186973021542161831690240000}$	$\frac{6642113669295531725816 3994783}{3682314032738752046039040000000}$

and use the binomial theorem to raise Eq. (B12) to power k. Employing the definition Eq. (B1) for the moments $U_{2j}(P_s)$ and $U_{2(k-j)}(P_{n-1-s})$, we obtain

$$U_{2k}(F_{n-1,s}) = \sum_{j=0}^{k} \binom{k}{j} U_{2j}(P_s) U_{2(k-j)}(P_{n-s-1}). \quad \text{(B13)}$$

Finally, substituting Eq. (B13) into Eq. (B11), we obtain the following relation for the even moments of P_n:

$$U_{2m}(P_n) = \frac{1}{n+2m} \sum_{s=0}^{n-1} \sum_{k=0}^{m} \sum_{j=0}^{k} \binom{n+1}{s+1} \binom{m}{k} \binom{k}{j} \times h_{n,s}^{2(m-k)+1} U_{2j}(P_s) U_{2(k-j)}(P_{n-s-1}). \quad \text{(B14)}$$

This recursion relation, together with the initial values $U_0(P_0) = 1$ and $U_{2m}(P_0) = 0$, for $m = 1, 2, 3, \ldots$, defines an arbitrary even-order moment.

In Tables II and III we give numerical and exact values for the even moments $\langle r^{2m} \rangle$ obtained from $U_{2m}(P_n)$, for dimensions $n < 16$. The un-normalized moments are computed using the recursion relation Eq. (B14).

```
h[n_,s_]:=h[n,s]=Sqrt[(s+1)(n-s)(n+1)]/2
U[m_,0]:=U[m,0]=If[m==0,1,0]
U[m_,n_]:=U[m,n]=Simplify[Sum[
 Binomial[n+1,s+1] Binomial[m,k] Binomial[k,j]
 h[n,s]^(2 m-2 k+1) U[j,s] U[k-j,n-s-1],
{s,0,n-1},{k,0,m},{j,0,k}]/(n+2 m)]
II[m_,n_]:=U[m,n]/U[0,n]
Mo[m_,n_]:=II[m,n](12 R^2/(n(n+1)(n+2)))^m
```

The normalized moments $I_{2m}(P_n)$ are then defined by Eq. (B1). Both of these follow the conventions of Conway and Sloane, Chapter 21, Sec. 3F [29]. They are then rescaled following Eq. (B2) with $d = 2m$ to obtain $\langle r^{2m} \rangle$, which are in the conventions used everywhere else in this paper.

The following lines of *Mathematica* are sufficient to calculate the arbitrary even moments $U_{2m}(P_n) = \mathrm{U[m, n]}$ up to dimensions of several thousand. The normalized moments are $I_{2m}(P_n) = \mathrm{II[m, n]}$, and the moments (with the length conventions used in the remainder of this paper, as they appear in Tables II and III) are $\langle r^{2m} \rangle = \mathrm{Mo[m, n]}$.

[1] L. A. Wainstein and V. D. Zubakov, *Extraction of Signals from Noise* (Dover, New York, 1970).

[2] C. W. Helstrom, *Statistical Theory of Signal Detection*, International series of monographs on electronics and instrumentation (Pergamon Press, New York, 1960).

[3] B. F. Schutz, Gravitational wave sources and their detectability, Classical Quantum Gravity **6**, 1761 (1989).

[4] B. S. Sathyaprakash and S. V. Dhurandhar, Choice of filters for the detection of gravitational waves from coalescing binaries, Phys. Rev. D **44**, 3819 (1991).

[5] B. F. Schutz, *The Detection of Gravitational Waves*, edited by D. G. Blair (Cambridge University Press, Cambridge, England, 1991), p. 406.

[6] C. Cutler *et al.*, The last three minutes: Issues in gravitational wave measurements of coalescing compact binaries, Phys. Rev. Lett. **70**, 2984 (1993).

[7] B. S. Sathyaprakash, Filtering post-Newtonian gravitational waves from coalescing binaries, Phys. Rev. D **50**, R7111 (1994).

[8] C. Cutler and E. E. Flanagan, Gravitational waves from merging compact binaries: How accurately can one extract the binary's parameters from the inspiral wave form?, Phys. Rev. D **49**, 2658 (1994).

[9] S. V. Dhurandhar and B. S. Sathyaprakash, Choice of filters for the detection of gravitational waves from coalescing binaries. 2. Detection in colored noise, Phys. Rev. D **49**, 1707 (1994).

[10] S. V. Dhurandhar and B. F. Schutz, Filtering coalescing binary signals: Issues concerning narrow banding, thresholds, and optimal sampling, Phys. Rev. D **50**, 2390 (1994).

[11] R. Balasubramanian and S. V. Dhurandhar, Performance of Newtonian filters in detecting gravitational waves from coalescing binaries, Phys. Rev. D **50**, 6080 (1994).

[12] R. Balasubramanian, B. S. Sathyaprakash, and S. V. Dhurandhar, Gravitational waves from coalescing binaries: Detection strategies and Monte Carlo estimation of parameters, Phys. Rev. D **53**, 3033 (1996); **54**, 1860(E) (1996).

[13] B. J. Owen and B. S. Sathyaprakash, Matched filtering of gravitational waves from inspiraling compact binaries: Computational cost and template placement, Phys. Rev. D **60**, 022002 (1999).

[14] B. Allen, W. G. Anderson, P. R. Brady, D. A. Brown, and J. D. E. Creighton, FINDCHIRP: An algorithm for detection of gravitational waves from inspiraling compact binaries, Phys. Rev. D **85**, 122006 (2012).

[15] L. Nieder, B. Allen, C. J. Clark, and H. J. Pletsch, Exploiting orbital constraints from optical data to detect binary gamma-ray pulsars, Astrophys. J. **901**, 156 (2020).

[16] B. P. Abbott *et al.* (LIGO Scientific, Virgo Collaborations), First low-frequency Einstein@Home all-sky search for continuous gravitational waves in Advanced LIGO data, Phys. Rev. D **96**, 122004 (2017).

[17] C. Messenger, R. Prix, and M. A. Papa, Random template banks and relaxed lattice coverings, Phys. Rev. D **79**, 104017 (2009).
[18] I. W. Harry, B. Allen, and B. S. Sathyaprakash, Stochastic template placement algorithm for gravitational wave data analysis, Phys. Rev. D **80**, 104014 (2009).
[19] B. Steltner, M. A. Papa, H.-B. Eggenstein *et al.*, Einstein@-home all-sky search for continuous gravitational waves in LIGO O2 public data, Astrophys. J. **909**, 79 (2021).
[20] B. P. Abbott, R. Abbott, T. D. Abbott *et al.* (LIGO Scientific and Virgo Collaborations), First low-frequency Einstein@-Home all-sky search for continuous gravitational waves in Advanced LIGO data, Phys. Rev. D **96**, 122004 (2017).
[21] J. Ming, M. A. Papa, A. Singh *et al.*, Results from an Einstein@Home search for continuous gravitational waves from Cassiopeia A, Vela Jr., and G347.3, Phys. Rev. D **100**, 024063 (2019).
[22] C. J. Clark, L. Nieder, G. Voisin *et al.*, Einstein@Home discovery of the gamma-ray millisecond pulsar PSR J2039-5617 confirms its predicted redback nature, Mon. Not. R. Astron. Soc. **502**, 915 (2021).
[23] L. Nieder, C. J. Clark, D. Kandel *et al.*, Discovery of a gamma-ray black widow pulsar by GPU-accelerated Einstein@Home, Astrophys. J. **902**, L46 (2020).
[24] L. Nieder, C. J. Clark, C. G. Bassa *et al.*, Detection and timing of gamma-ray pulsations from the 707 Hz pulsar J0952-0607, Astrophys. J. **883**, 42 (2019).
[25] B. Allen, Optimal template banks, Phys. Rev. D **104**, 042005 (2021).
[26] B. J. Owen, Search templates for gravitational waves from inspiraling binaries: Choice of template spacing, Phys. Rev. D **53**, 6749 (1996).
[27] B. Allen, Spherical ansatz for parameter-space metrics, Phys. Rev. D **100**, 124004 (2019).
[28] K. Wette, Empirically extending the range of validity of parameter-space metrics for all-sky searches for gravitational-wave pulsars, Phys. Rev. D **94**, 122002 (2016).
[29] J. H. Conway and N. J. A. Sloane, *Sphere Packings, Lattices and Groups* (Springer, Berlin, 1999).
[30] R. Prix, Template-based searches for gravitational waves: Efficient lattice covering of flat parameter spaces, Classical Quantum Gravity **24**, S481 (2007).
[31] M. D. Sikiric, A. Schuermann, and F. Vallentin, A generalization of Voronoi's reduction theory and its application, Duke Math. J. **142**, 127 (2008).
[32] S. S. Ryshkov and E. P. Baranovskii, Solution of the problem of least dense lattice covering of five-dimensional space by equal spheres, Dokl. Akad. Nauk. **222**, 39 (1975).
[33] B. Knispel and B. Allen, Blandford's argument: The strongest continuous gravitational wave signal, Phys. Rev. D **78**, 044031 (2008).
[34] L. Wade, X. Siemens, D. L. Kaplan, B. Knispel, and B. Allen, Continuous gravitational waves from isolated galactic neutron stars in the advanced detector era, Phys. Rev. D **86**, 124011 (2012).
[35] J. Mathews and R. L. Walker, *Mathematical Methods of Physics* 2nd ed. (Addison-Wesley, New York, 1970).
[36] M. D. Perlman, Jensen's inequality for a convex vector-valued function on an infinite-dimensional space, J. Multivariate Anal. **4**, 52 (1974).
[37] See Supplemental Material at http://link.aps.org/supplemental/10.1103/PhysRevD.104.122007 for *Mathematica* script to compute the even moments of the $\mathbb{Z}^n$ lattice (Appendix A).